Uniqueness of Multiangular Measurements—Part II: Joint Retrieval of Vegetation Structure and Photosynthetic Activity From MISR

Nadine Gobron, *Member, IEEE*, Bernard Pinty, Michel M. Verstraete, *Member, IEEE*, Jean-Luc Widlowski, and David J. Diner, *Associate Member, IEEE*

Abstract—The Multi-angle Imaging SpectroRadiometer (MISR) instrument on board the Terra platform offers the capability of acquiring reflectance data on any earth target in four spectral bands, from nine different directions, in at most seven minutes, at a spatial resolution adequate for the monitoring of the status of terrestrial surfaces. This paper describes the implementation of a physical and mathematical approach to design a simple two-dimensional algorithm dedicated to the interpretation of data collected by this instrument. One dimension fully exploits the spectral information in the blue, red and near-infrared bands while the other dimension capitalizes on the multi-angular capability of MISR to assess the anisotropic behavior of terrestrial surfaces with respect to solar radiation. The spectral information is derived following an approach proposed for single angle instruments, such as the MEdium Resolution Imaging Spectrometer (MERIS), the Global Imager (GLI), the Sea-viewing Wide Field-of-view Sensor (SeaWIFS) and VEGETATION. The access to simultaneous multiangular observations from MISR allows extending this approach. This strategy delivers an estimate of the Fraction of Absorbed Photosynthetically Active Radiation (FAPAR), which pertains to vegetation photosynthetic activity and is a measure of the presence and density of vegetation. As shown in Part I, the angular shape of the reflectance is strongly related to the architecture of the vegetation and, under some favorable conditions, permits an assessment of surface heterogeneity. The proposed VEGetation Activity and Structure (VEGAS) algorithm for MISR therefore delivers two axes of information representing a) FAPAR and b) vegetation structure at MISR subpixel resolution. Its application should improve the present knowledge of vegetation characteristics at regional and global scales.

Index Terms—FAPAR, MISR, surface heterogeneity, VEGAS, vegetation index.

I. INTRODUCTION

THE Multi-angle Imaging SpectroRadiometer (MISR) instrument on board NASA's Terra platform acquires reflectance data from any earth target in four solar spectral bands, from nine different directions, in at most seven minutes, at a spatial resolution of 275 m in all bands of the nadir camera and in the red band of the off-nadir cameras, and 1.1 km in the remainder (see [1]). This configuration is used globally and is referred to as global mode. The MISR instrument thus samples the earth's reflectance field along two independent but complementary spectral and angular axes. The spectral sampling capitalizes on the heritage of previous multispectral, single-angle sensors, while the angular sampling at medium spatial resolution offers new and unprecedented opportunities to document the state and evolution of land surfaces. Specifically, this observational strategy 1) improves the accuracy of products derived on the sole basis of the spectral sampling, e.g., Leaf Area Index (LAI) and Fraction of Absorbed Photosynthetically Active Radiation (FAPAR) (see, for instance, [2]–[4]), and 2) permits the extraction of geophysical products that exploits the anisotropy of the coupled surface-atmosphere geophysical system (see [5], hereafter referred to as Part I). The VEGetation Activity and Structure (VEGAS) algorithm described here simultaneously retrieves measures of the vegetation photosynthetic activity and the structure of plant canopies from MISR data.

The spectral signature of land surfaces is exploited to derive information on FAPAR, along the lines of the methodology derived previously for a series of single-angle multispectral sensors such as MERIS [6], GLI, VEGETATION [7], and SeaWIFS [8]. This methodology recognizes the anisotropic behavior of the BRF fields and implements a mean spectral anisotropic pattern assumed to be appropriate for any geophysical situation. However, use of MISR spectral data at multiple view angles translates into more reliable and accurate FAPAR products [1], [4].

The angular signature is additionally used to obtain information on the geometric and physical properties of the environment. As shown in the accompanying paper (Part I), the structure of the environment, specifically subpixel scale heterogeneity, may be revealed under favorable conditions of illumination. The algorithm also incorporates a practical approach to decontaminating the measured angular signatures from atmospheric scattering effects.

This paper describes in detail how the spectral and angular data from the MISR instrument are exploited to retrieve information on the structure and photosynthetic activity of terrestrial surfaces. Section II explains the methodology we adopted to design the VEGAS algorithm. Results from a series of applications conducted on the basis of actual MISR data are discussed in the last section.

II. DESIGN OF THE MISR VEGETATION ACTIVITY AND STRUCTURE (VEGAS) ALGORITHM

The VEGAS algorithm uses top of the atmosphere (TOA) radiances from MISR to estimate the amplitude factors of the bidirectional reflectance factors (BRFs), at the top of the canopy (TOC), for the red and near-infrared bands. These amplitude factors are in turn used to estimate FAPAR, and the anisotropy shape factor, the $k_{\text{red}}^{\text{SFC}}$ parameter is used to provide the information about heterogeneity discussed in Part I. The expressions used for these estimates are in the form of polynomials whose coefficients are obtained by optimal fitting to training data generated by atmospheric and surface radiation transfer calculations [9]: the red and near-infrared amplitude factors at the TOC (called the rectified reflectances) are obtained from the TOA radiances measured in the blue, red, and near-infrared part of the solar spectrum. Because the blue band is most sensitive to atmospheric scattering, it is used to remove the effects of variable atmospheric transmission factors from the MISR radiances. The FAPAR is in turn obtained from a polynomial in the estimates of TOC red and near-infrared BRF amplitude factors. Finally, the TOC anisotropy shape factor, $k_{\text{red}}^{\text{SFC}}$, is estimated from the $k_{\text{red}}^{\text{TOA}}$ parameter value and the BRF asymmetry shape, $\Theta_{\text{red}}^{\text{TOA}}$, parameter value.

The first step of our methodology is thus to simulate sensor-like or training data sets of BRFs for a variety of geophysical scenarios with detailed radiation transfer models. Second, the coefficients of two *ad hoc* polynomial formulae are optimized to generate so-called rectified reflectances at the red and near-infrared wavelengths to minimize atmospheric and angular perturbations. These two rectified reflectances are then combined together in a third step to produce the final FAPAR formulae which optimally matches the values of the FAPAR simulated for the ensemble of geophysical scenarios included in the training data set.

The geophysical scenarios we generated to optimally retrieve a set of polynomial formulae are the same as those considered in previous studies by [7]. These scenarios are replicated in Table I for the convenience. They represent a wide range of vegetation, soil and atmosphere conditions and permit us to generate two axes of information which are insensitive to a number of geophysical perturbations. The training BRF data sets were designed to mimic MISR observations both from a spectral and angular point of view (see Table II). This simulated data set serves as a basis for deriving the optimal formulae required to estimate values composing the FAPAR and the structure axes, respectively.

A. The FAPAR Axis

The retrieval of FAPAR follows an approach analogous to the one adopted for the design of optimized indices suited for a series of single-angle sensors. It exploits a set of formulae to estimate the FAPAR values on the basis of the spectral and angular measurements collected at the top of the atmosphere by the MISR instrument.

The mathematical approach presented in Sections II-A1 and B is suited for use with 275-m and 1.1-km spatial resolution data

TABLE I
GEOPHYSICAL SCENARIOS USED TO CONSTRUCT THE TRAINING DATA SET

Medium	Variable	Values
Atmosphere model (Vermote *et al.*, 1997)	Aerosol optical thickness for a continental model	0.05, 0.3 and 0.8
Vegetation model	Leaf Area Index	0, 0.5, 1, 2, 3, 4, and 5
	Height of Canopy	0.5 m and 2 m
(Gobron *et al.*, 1997)	Equivalent ∅ of single leaf	0.01 m and 0.05 m
	Leaf Angle Distribution	Erectophile, Planophile
Soil data base (Price, 1995)	Soil reflectance	5 soil spectra, from dark to bright

TABLE II
ILLUMINATION AND OBSERVATION GEOMETRIES USED TO SIMULATE THE MISR RADIANCE FIELDS

Angle	Values
Solar zenith angle	20° and 50°
View zenith angle	0°, ± 26°, ± 45°, ± 60°, ± 70°
Sun-satellite relative azimuth	0°, 90° and 180°

from the nine MISR cameras. However, the availability of additional measurements at 275-m resolution in all bands of the nadir camera offers an alternative option using only spectral measurements from this camera. This single-angle approach, which is analogous to previous investigations conducted for a series of polar-orbiting satellites (see [7]), is summarized in Appendix I of this paper.

1) Mathematical Approach: The mathematical approach uses the following set of polynomial functions, noted $g_n(x, y)$, which are assumed to be appropriate to generate the rectified red band reflectances $(n = 1)$, the rectified near-infrared band reflectances $(n = 2)$ and the final formulae representing the FAPAR axis $(n = 0)$:

$$g_n(x, y) = f_n(x, y; l_{(n,1)}, \ldots, l_{(n,m)}) \tag{1}$$

where $l_{(n,m)}$ are the coefficients of the polynomial functions and x and y are two spectral variables, depending on the step being implemented.

The final formula is generated on the basis of the rectified band values, namely $\rho_{R\text{red}}$ and $\rho_{R\text{nir}}$ for the red and near-infrared bands, respectively:

$$\text{FAPAR} = g_0(\rho_{R\text{red}}, \rho_{R\text{nir}}) \tag{2}$$

with

$$\rho_{R\text{red}} = g_1 \left[\tilde{\rho}_0(\lambda_{\text{blu}}), \tilde{\rho}_0(\lambda_{\text{red}}) \right] \tag{3}$$

$$\rho_{R\text{nir}} = g_2 \left[\tilde{\rho}_0(\lambda_{\text{blu}}), \tilde{\rho}_0(\lambda_{\text{nir}}) \right] \tag{4}$$

where $\tilde{\rho}_0(\lambda_i)$ corresponds to the optimal value of the amplitude parameter of the BRF field derived from the RPV model [Part I, Eq. (1)] at the spectral band i. The value of this parameter can be optimally retrieved using a fast inversion scheme of the RPV

model fully described in [10] and summarized in Appendix II of this paper. This optimal retrieval also permits associating with $\tilde{\rho}_0(\lambda_i)$ the parameters $k(\lambda_i)$ and $\Theta(\lambda_i)$ that control the shape of the angular field of BRF (this is assuming that the value of the hot spot parameter $\rho_c(\lambda_i)$ can be approximated by the $\rho_0(\lambda_i)$ value [11]. For a given user defined accuracy, this procedure delivers consistent sets of $\tilde{\rho}_0(\lambda_i)$, $\tilde{k}(\lambda_i)$, and $\tilde{\Theta}(\lambda_i)$ values that best fit the BRF fields in the blue, red, and near-infrared bands, respectively. The inversion scheme can be applied to both the simulated and measured MISR spectral BRF fields at the top of the atmosphere.

The generic polynomial formula used for parameterizing the functions g_1 and g_2 is given by

$$
\begin{aligned}
&f_n(x, y; l_{(n,1)}, \ldots, l_{(n,m)}) \\
&= \frac{l_{n,1}(x + l_{n,2})^2 + l_{n,3}(y + l_{n,4})^2 + l_{n,5}xy}{l_{n,6}(x + l_{n,7})^2 + l_{n,8}(y + l_{n,9})^2 + l_{n,10}xy + l_{n,11}} \\
&(n = 1, 2)
\end{aligned} \tag{5}
$$

and the polynomial formula adopted for the final function g_0 is

$$
f_0(x, y; l_{(0,1)}, \ldots, l_{(0,m)}) = \frac{(l_{0,1}y - l_{0,2}x - l_{0,3})}{(l_{0,4} - x)^2 + (l_{0,5} - y)^2 + l_{0,6}}. \tag{6}
$$

The values of the m coefficients $l_{(n,m)}$ of each polynomial function g_n are estimated once and for all using an optimization procedure which minimizes the following cost function for polynomials g_1 and g_2:

$$
\begin{aligned}
\delta_{g_n}^2 = \sum_{\zeta_\lambda} \Big[g_n \left(\tilde{\rho}_0(\lambda_{\mathrm{blu}})^{\mathrm{TOA}}, \tilde{\rho}_0(\lambda_i)^{\mathrm{TOA}} \right) \\
- \tilde{\rho}_0(\lambda_i)^{\mathrm{SFC}} \Big]^2 \to 0 \quad (n = 1, 2)
\end{aligned} \tag{7}
$$

where ζ_λ represents the domain within the spectral space where the optimization is sought. This cost function forces the polynomial functions g_1 and g_2 to deliver rectified values which are as close as possible to the optimal value of the amplitude parameter of the BRF derived from the RPV model, namely $\tilde{\rho}_0(\lambda_i)$, estimated at the top of the canopy (SFC) for every surface and atmospheric condition included in the training BRF data sets.

The formula delivering the values of the FAPAR axis is then derived from a combination of these rectified channel values as expressed by (2). The coefficients $l_{(0,m)}$ of the final polynomial g_0 are determined in an optimal manner using the following cost function:

$$
\delta_{g_0}^2 = \sum_{\zeta} \left[g_0(\rho_{R\mathrm{red}}, \rho_{R\mathrm{nir}}) - \mathrm{FAPAR} \right]^2 \to 0. \tag{8}
$$

According to the mathematical approach presented in this section, the formula representing the FAPAR axis is constrained to deliver values which are close to those FAPAR values associated with the ensemble of canopy types implemented in the training data sets. In the present application, the slight sensitivity of the FAPAR with respect to the sun zenith angle has been neglected and the optimization was performed using sun zenith angle values of $20°$ and $50°$ together.

TABLE III
OPTIMAL VALUES OF THE COEFFICIENTS FOR THE POLYNOMIAL g_1

$l_{1,1}$	$l_{1,2}$	$l_{1,3}$	$l_{1,4}$	$l_{1,5}$
0.01753	−0.02867	−0.003229	0.06350	−0.01359
$l_{1,6}$	$l_{1,7}$	$l_{1,8}$	$l_{1,9}$	$l_{1,10}$
-0.000176	2.5085	−0.017928	0.02268	0.006939
$l_{1,11}$				
0.0				

TABLE IV
OPTIMAL VALUES OF THE COEFFICIENTS FOR THE POLYNOMIAL g_2

$l_{2,1}$	$l_{2,2}$	$l_{2,3}$	$l_{2,4}$	$l_{2,5}$
−2.02890	0.09309	0.6653	0.3796	2.6731
$l_{2,6}$	$l_{2,7}$	$l_{2,8}$	$l_{2,9}$	$l_{2,10}$
0	0	0	0	0
$l_{2,11}$				
1.0				

TABLE V
OPTIMAL VALUES OF THE COEFFICIENTS FOR THE POLYNOMIAL g_0

$l_{0,1}$	$l_{0,2}$	$l_{0,3}$	$l_{0,4}$	$l_{0,5}$	$l_{0,6}$
0.3932	0.4876	−0.02827	−0.1622	0.2459	0.1103

2) Results and Evaluation: Equations (7) and (8) were solved successively using an optimization procedure which allows us to derive numerical coefficients of the polynomial formulae. The values of the optimal coefficients for g_1, g_2 and g_0 are given in Tables III–V, respectively.

Fig. 1 illustrates the performances of the two step procedure we developed to retrieve FAPAR on the basis of spectral TOA BRF fields measured by MISR. The top panels show the scatterplots between the actual amplitude of the surface BRF derived from the inversion of the RPV model, namely $\tilde{\rho}_0(\lambda_i)^{\mathrm{SFC}}$, against the corresponding values delivered by the rectification procedure, in the red and near-infrared spectral bands, respectively. According to (7), a perfect rectification would project all points of these two panels on the one-to-one line. It can be seen that the rectification procedure is quite successful in limiting any large dispersion or biases induced by the coupled surface-atmosphere effects on the ensemble of TOA BRFs considered in the training data set. The overall ability of both the rectification procedure applied to the red and near-infrared BRFs and the optimal combination used to derive the final formula, namely g_0, to provide an estimate of FAPAR is shown on the bottom
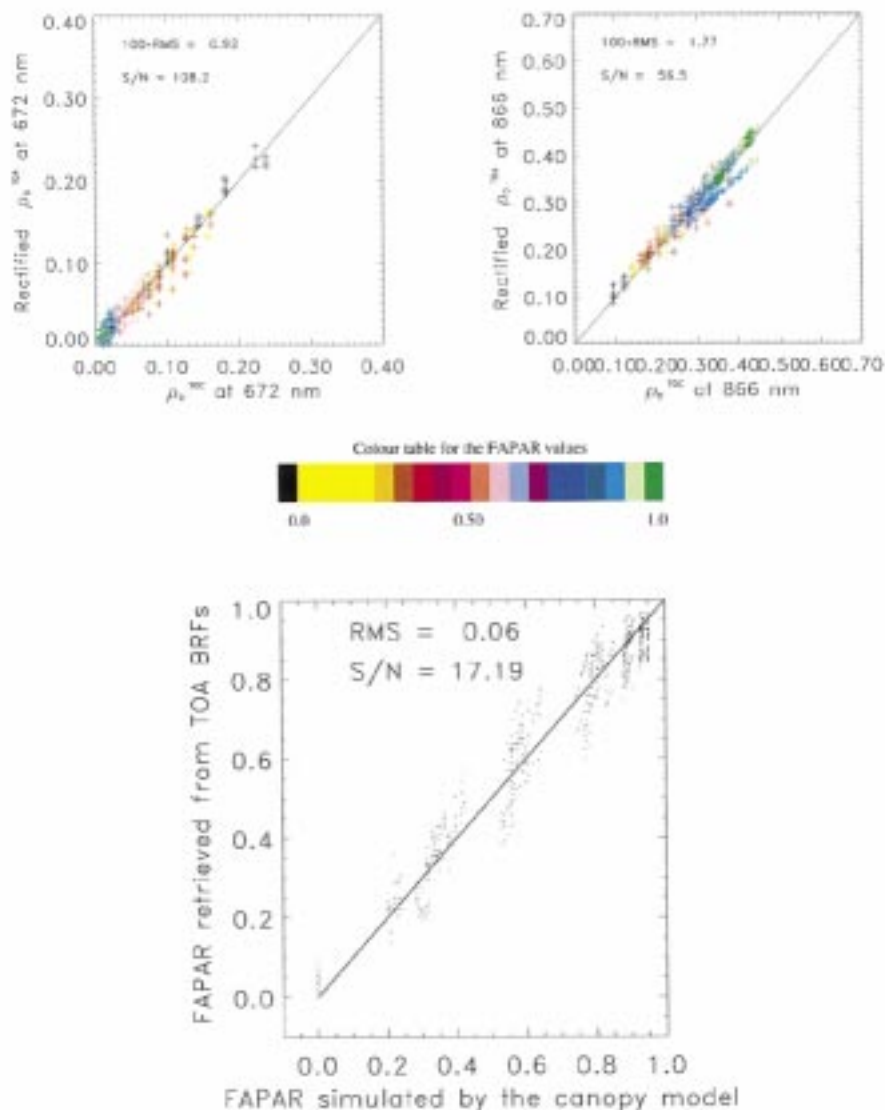
Fig. 1. Results of the rectification procedure of the red (top left panel) and near-infrared (top right panel) bands of the MISR sensor. The bottom panel shows the scatterplot between the FAPAR values derived from the FAPAR formula against actual values corresponding to the various geophysical scenarios implemented in the training data set. The color code indicates simulations achieved for the different FAPAR values. RMS and SNR stand for root mean square and signal-to-noise ratio, respectively.

panel of Fig. 1. The relationship between FAPAR values derived from the formula and those associated with the geophysical scenarios exhibits a root mean square error (RMS) of 0.06 with a signal-to-noise ratio (SNR) (see [12]) value close to 17. The robustness of our approach with respect to changes in the atmospheric type and aerosol load, as well as to three-dimensional (3-D) structures that were not included into the training data set, was extensively examined and discussed in [7] for a series of single-angle sensors, and similar conclusions apply in the present study.

The AirMISR data set collected over the Konza prairie site which has already been used in Section IV of Part I offers one more opportunity to test the robustness of our approach with respect to atmospheric effects. A surface BRF data set was derived on the basis of the measured TOA BRF spectral fields using the atmospheric correction procedure described in Part I. Therefore, both BRF data sets, at TOA and surface levels, could be used as inputs to the series of polynomial functions we opti-

mized to generate the estimated FAPAR axis. A perfect insensitivity of the FAPAR estimation with respect to atmospheric effects would thus translate into the production of quite similar FAPAR maps over the Konza prairie from these two very different data sets. This quality check was performed on those pixels for which the spectral BRF data strings satisfied a series of screening tests indicated in Table VI. These tests are applied sequentially to identify vegetated pixels, and only those pixels for which the FAPAR value is larger than zero are considered further. The results of these procedures are displayed in Fig. 2. A visual comparison of results derived from the surface (top panel) and the TOA (bottom panel) BRF data sets overall reveals a very good agreement between these two estimates. Indeed, Fig. 3 shows that there is no systematic bias between these two estimates and the RMS value, which is close to 0.06, indicates a limited scatter of the distributions. This experiment illustrates and confirms that the FAPAR axis is almost insensitive to, at least, clear sky atmospheric conditions.

TABLE VI
DATA SCREENING TESTS

| Spectral [a] and angular [b] tests	Associated categories
$0 < \rho_{blue} < 0.3$ and $0 < \rho_{red} < 0.5$ and $0 < \rho_{nir} < 0.7$ and $0 < \rho_{blue} \leq \rho_{nir}$ and $\rho_{nir} \geq 1.25\,\rho_{red}$	vegetated surface
$\rho_{blue} \leq 0$ or $\rho_{red} \leq 0$ or $\rho_{nir} \leq 0$	bad pixels
$\rho_{blue} \geq 0.3$ or $\rho_{red} \geq 0.5$ or $\rho_{nir} \geq 0.7$	cloud, snow and ice
$0 < \rho_{blue} < 0.3$ and $0 < \rho_{red} < 0.5$ and $0 < \rho_{nir} < 0.7$ and $\rho_{blue} > \rho_{nir}$	water body, deep shadow and miscellaneous
$0 < \rho_{blue} < 0.3$ and $0 < \rho_{red} < 0.5$ and $0 < \rho_{nir} < 0.7$ and $0 < \rho_{blue} < \rho_{nir}$ and $1.25\,\rho_{red} > \rho_{nir}$	bright surface
$\rho_{Rred} < 0$ or $\rho_{Rnir} < 0$	undefined
$\epsilon_{fit} > 10\%$ [c]	poor fit of RPV over all cameras

a Spectral tests applied to the Af, Aa, and An Cameras.
b Angular test applied to all cameras all spectral bands.
c Defined in (15) (Appendix II).

B. The Structure Axis

MISR offers the ability to document the anisotropic behavior of the BRF fields and, thus, to characterize different surface types based upon their angular signature only. Moreover, as discussed in Part I, the value of the parameter k_{red}, estimated from the inversion of the RPV model against the BRF field acquired at the red wavelength, can further be used to expose surface heterogeneity at the subpixel scale. This interpretation is supported by the analysis of BRF data strings collected by the AirMISR instrument and processed in order to reduce as much as possible the effects of atmospheric contamination. The latter processing step was justified since the presence of any scattering turbid media above the surface would bias the BRF anisotropy pattern toward a bowl-shape and thus would decrease the value of the k_{red}^{SFC} parameter. Indeed, as explained in Section II-B of Part I, turbid media such as the atmosphere tend to hide the surface heterogeneity associated with k_{red}^{SFC} values larger than unity.
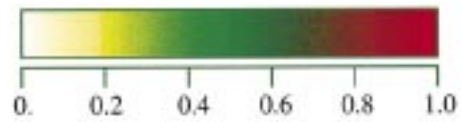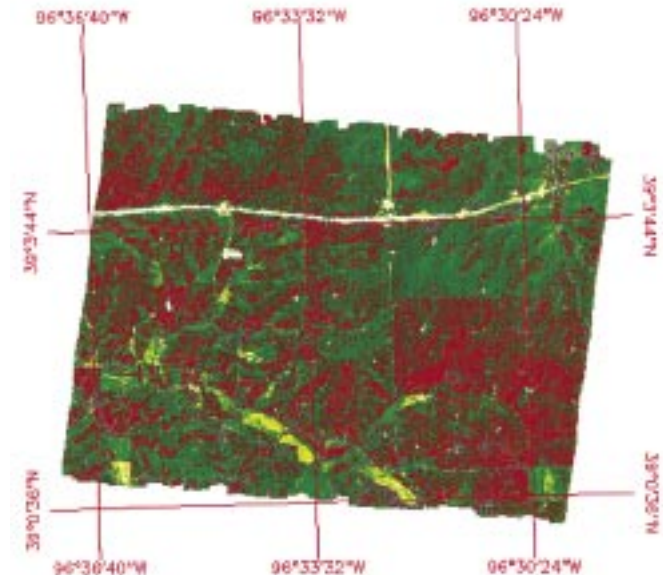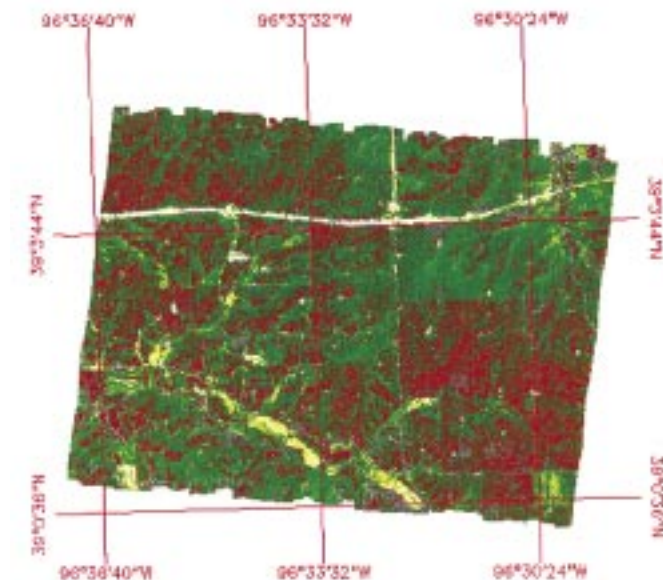

Fig. 2. FAPAR maps derived with surface (top panel) and TOA (bottom panel) BRF data collected in the blue, red and near-infrared bands of the AirMISR instrument over Konza prairie on July 13, 1999. The color code goes from yellow tones for very low vegetation cover/activity to red tones for dense green vegetation. The grey color identifies screened pixels according to the tests given in Table VI.

Directional atmospheric effects are documented in Fig. 4, which shows graphical examples of the progressive changes in the BRF anisotropy shapes generated for various aerosol optical thickness values. The top (bottom) panel corresponds to BRF
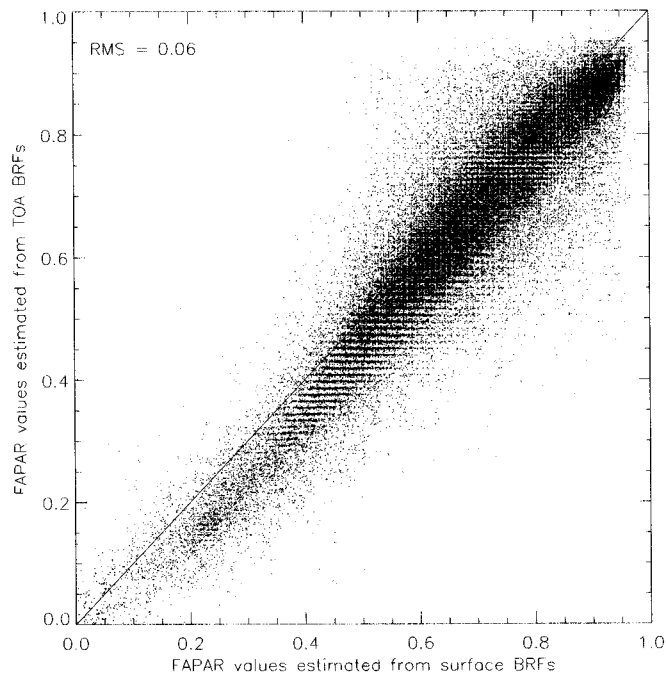
Fig. 3. Comparison between the FAPAR values derived from TOA and surface BRFs. The data sets are the same as in Fig. 2. RMS stands for the root mean square of the relationship between the two FAPAR distributions.
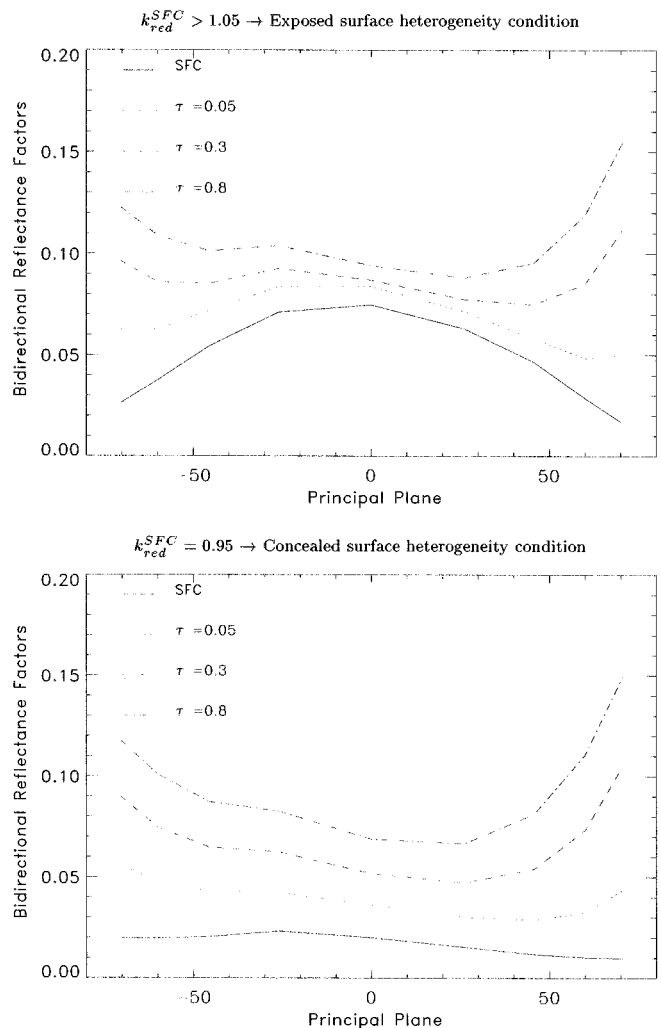

Fig. 4. Example of the changes in the BRF anisotropy patterns and the associated k_{red} values due to the presence of various atmospheric conditions featured by three aerosol optical thickness values (at 550 nm) set at 0.05, 0.3, and 0.8. These simulations are extracted from the large ensemble generated for designing the training data set (see Table I). The top (bottom) panel corresponds to low (large) leaf area index conditions favoring the exposure (concealment) of the surface heterogeneity.

fields simulated in the red band in the principal plane for surface conditions where the heterogeneity is exposed (concealed) as discussed in Part I. The atmospheric conditions used to generate these plots follow from those described in Table I when producing the training data set. The variations in the values of the parameter k_{red} associated with changes in aerosol load clearly confirm the expected contribution due to the addition of turbid layers above the surfaces. In the worst case scenario considered here, a continental aerosol atmosphere with $\tau_{550\,\mathrm{nm}} = 0.8$, the TOA BRF shapes fully mask the specific surface anisotropy pattern of the BRF and the two surface types become undistinguishable on the basis of their anisotropic patterns only.

An additional illustration of the bias induced by the atmosphere on the k_{red} parameter values is given in Fig. 5 which shows, on the top (bottom) panel, the map of the parameter k_{red} derived from the TOA (surface) BRF data set. The results displayed on these two panels illustrate the magnitude of the bias induced by atmospheric effects, under low aerosol load conditions, on the values of the $k_{\mathrm{red}}^{\mathrm{SFC}}$ parameter. The reddish hue of the map derived from TOA BRFs (top panel) illustrates this bias which clearly opposes the potential exposure of surface heterogeneity detected from the analysis of surface BRFs (bottom panel).

From these series of examples, it appears that the proper characterization of the intrinsic surface anisotropic behavior, with respect to a given solar illumination condition, requires the removal of the perturbing atmospheric effects. For all practical purposes, we are then left with the requirement to design a computationally efficient technique to approximate the $k_{\mathrm{red}}^{\mathrm{SFC}}$ parameter values from the corresponding values $k_{\mathrm{red}}^{\mathrm{TOA}}$ estimated on the basis of the BRF fields measured in the red band. The assessment of the $k_{\mathrm{red}}^{\mathrm{SFC}}$ values on the basis of TOA measurements technically follows from an approach analogous to the one we adopted in Section II-A to derive the FAPAR axis formula. In the context of the estimation of the surface anisotropy pattern, i.e., the k_{red} parameter values, a series of tests was conducted in order to identify the most appropriate information which could yield a reliable and computationally efficient rectification of the $k_{\mathrm{red}}^{\mathrm{TOA}}$ values. This information must satisfy a number of conditions including an ability to change significantly and systematically with the atmospheric conditions. Over land vegetation, the parameter $\Theta_{\mathrm{red}}^{\mathrm{TOA}}$ derived from the inversion the RPV model against the TOA BRF measured in the red band of MISR was found appropriate to conduct the rectification task of the values of the k_{red} parameter. Indeed, almost independent of surface type, the increase in the atmospheric aerosol load enhances the scattering of radiation in the forward direction at the top of the atmosphere. Consequently, this feature translates into a systematic bias of the RPV model parameter $\Theta_{\mathrm{red}}^{\mathrm{TOA}}$ toward large positive values although some dependency with respect to the scattering plane is anticipated.

$\longleftarrow$ Bowl-shape   Bell-shape $\longrightarrow$

0.5   1.   1.5

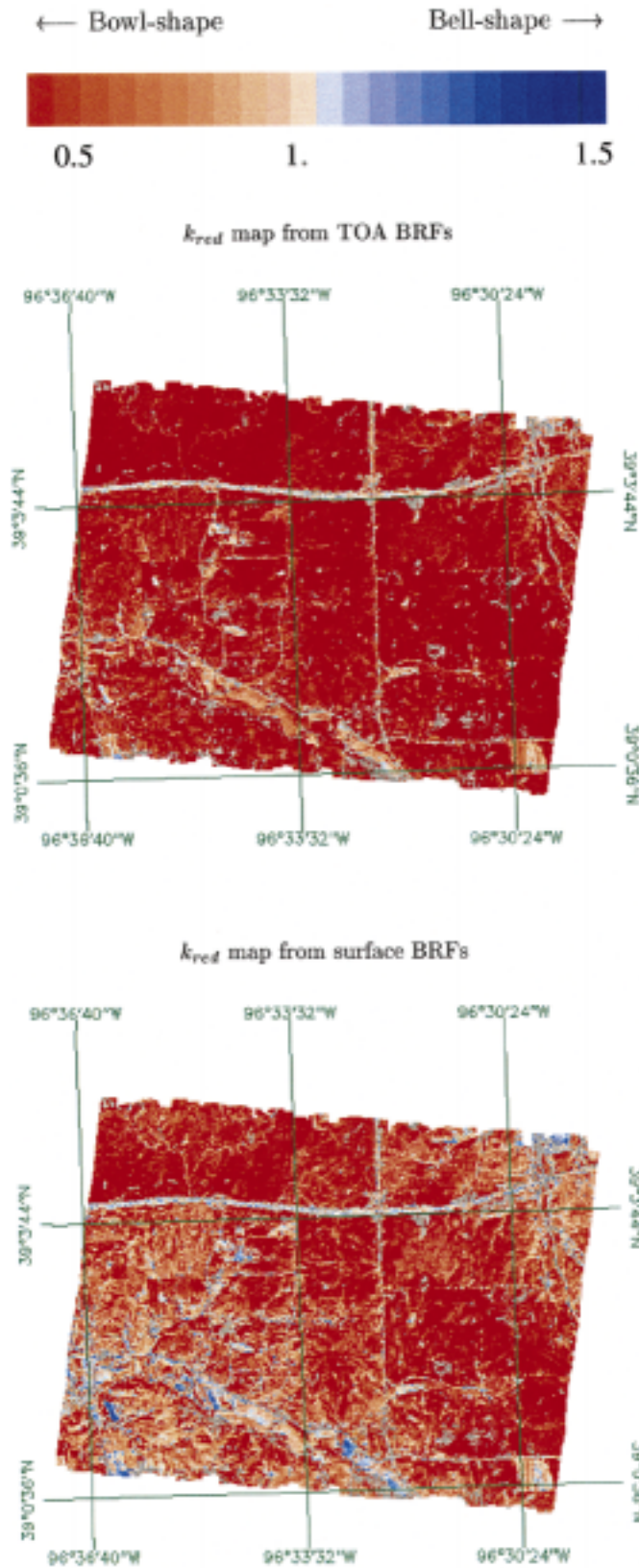k_{red} map from TOA BRFs

k_{red} map from surface BRFs

Fig. 5.   Illustration of the bias induced by the atmosphere on the values of the parameter k_{red}. These values are obtained from an inversion of the RPV model against the BRF data sets collected in the red band of the AirMISR instrument over Konza prairie on July 13, 1999. The top panel shows the map of the parameter k_{red} derived from the TOA BRF data set. The bottom panel shows the map of the parameter k_{red} derived from the surface BRF data set.

TABLE VII
OPTIMAL VALUES OF THE COEFFICIENTS FOR THE POLYNOMIAL g_3

$l_{3,1}$	$l_{3,2}$	$l_{3,3}$	$l_{3,4}$
-1.0885	0.74143	3.2805	-1.7135

1) Mathematical Approach: The mathematical implementation of the rectification procedure assumes that, as was done in Section II-B, a simple polynomial function $g_n \left(k_{\mathrm{red}}^{\mathrm{TOA}}, \Theta_{\mathrm{red}}^{\mathrm{TOA}} \right)$ is appropriate for this task. It was also assumed that the MISR training data set presented in Tables I and II permits us to optimize the polynomial formula and its numerical coefficients. This optimization step requires imposing a cost function in order to force the polynomial function g_3 to deliver rectified values of the $k_{\mathrm{red}}^{\mathrm{TOA}}$ parameter which are as close as possible to the associated values of $k_{\mathrm{red}}^{\mathrm{SFC}}$ at the surface level. This cost function can be expressed as follows:

$$\delta_{g_3}^2 = \sum_{\zeta_{\mathrm{red}}} \left[g_3 \left(k_{\mathrm{red}}^{\mathrm{TOA}}, \Theta_{\mathrm{red}}^{\mathrm{TOA}} \right) - k_{\mathrm{red}}^{\mathrm{SFC}} \right]^2 \to 0 \qquad (9)$$

where ζ_{red} represents the angular domain covered in the training data set where the optimization is applied.

2) Results and Evaluation: In order to derive an acceptable solution for (9), the following formula was adopted for $g_3(x, y)$:

$$f_3(x, y; l_{(3,1)}, \ldots, l_{(3,m)}) = l_{3,1} y^2 - l_{3,2} x^2 - \frac{l_{3,3} x}{y + l_{3,4}} \quad (10)$$

where x and y represent the values of parameter $k_{\mathrm{red}}^{\mathrm{TOA}}$ and $\Theta_{\mathrm{red}}^{\mathrm{TOA}}$, respectively. The values of the m optimal coefficients $l_{(3,m)}$ entering the polynomial formula are given in Table VII.

Fig. 6 illustrates the various steps of the rectification procedure that best estimates the values of the parameter at the surface level, $k_{\mathrm{red}}^{\mathrm{SFC}}$, from the values derived using TOA BRF data. The top left (right) panel shows the scatterplots between these two quantities before (after) applying the rectification procedure. It can be seen that this procedure reduces bias of the original distributions and tends to regroup the points around the one-to-one line. It is however noticeable that this procedure is less successful for geophysical conditions yielding values of $k_{\mathrm{red}}^{\mathrm{SFC}}$ which are larger than unity.

The series of isolines, which are associated to the polynomial g_3 in the $(k_{\mathrm{red}}, \Theta_{\mathrm{red}})$ space for a variety of atmospheric conditions, are shown in the bottom panel of Fig. 6. This panel also illustrates the variations of the values of the parameter Θ_{red} with the aerosol optical thickness τ. A "perfect" set of isolines would ensure that all symbols of the same color are uniquely linked together so that each isoline value would correspond exactly to the values of the parameter $k_{\mathrm{red}}^{\mathrm{SFC}}$ estimated in the absence of atmospheric contamination. The rectification procedure, based on polynomial g_3, approximates this ideal case. It establishes the series of isolines which link together the values of the k_{red} parameter for each surface type (different color tones are assigned to different Leaf Area Index
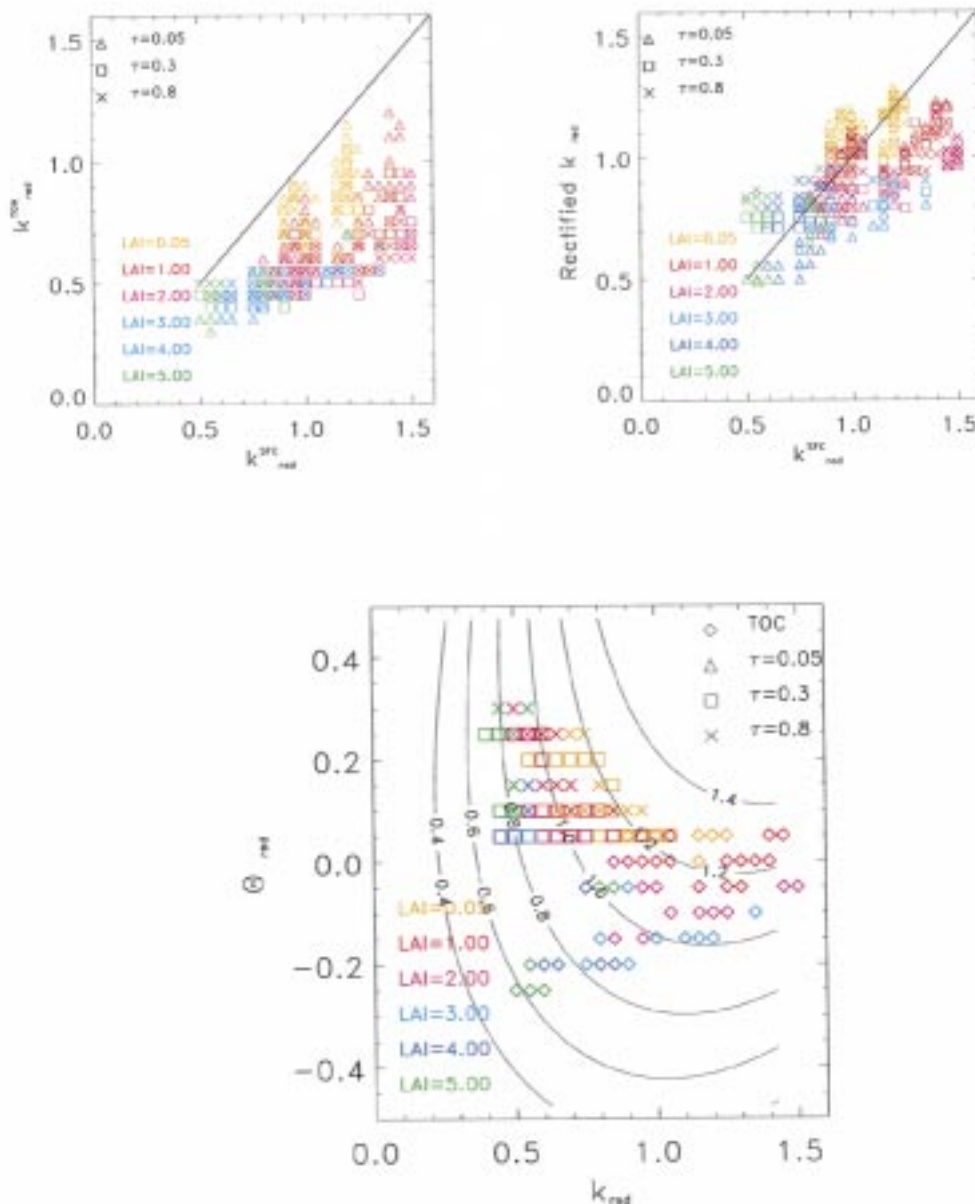
Fig. 6.   Results of the rectification procedure (before (after) on the top left (right) panels) of the k_{red} values on the basis of the parameter Θ estimated by the inversion of the RPV model against TOA BRFs simulated in the red band. The bottom panel represents the isolines delivered by the polynomial g_3 in the (k_{red}, Θ_{red}) space. Each color (symbol) indicates the various surface (aerosol) conditions imposed in the training data set (see Table I).

conditions) under various atmospheric conditions (featured by the different symbols). The performance of the proposed rectification could be further improved and generalized at the costs of implementing a more complex polynomial formula ingesting the nadir measurements in the blue and red bands, as was done Section II-A.

The performance of the proposed rectification of the k_{red} parameter can be assessed on the basis of the data set collected by the AirMISR instrument over the Konza prairie and further decontaminated from atmospheric perturbations (see Section IV in Part I). Fig. 7 (top panel) displays the map of the rectified values of the k_{red} parameter obtained from the procedure described above. The comparison of these results with those al-

ready shown in Fig. 5 (bottom panel) indicates that the main surface features already described in Part I, notably the transitions from bowl to bell-shaped anisotropy patterns, are reasonably well recovered. Moreover, the scatterplot between these two sets of values (bottom panel of Fig. 7) confirms that no systematic bias is induced by the rectification procedure.

The simple and low cost procedure presented in this section thus permits us to approximate k_{red}^{SFC} parameter over land vegetated regions. As explained in Part I, this parameter is directly linked to the surface structure and, given the highest spatial resolution of the MISR instrument available, i.e., 275 m, most of this information should be related to vegetation structure. It was also shown in Part I that, under favorable conditions, this parameter
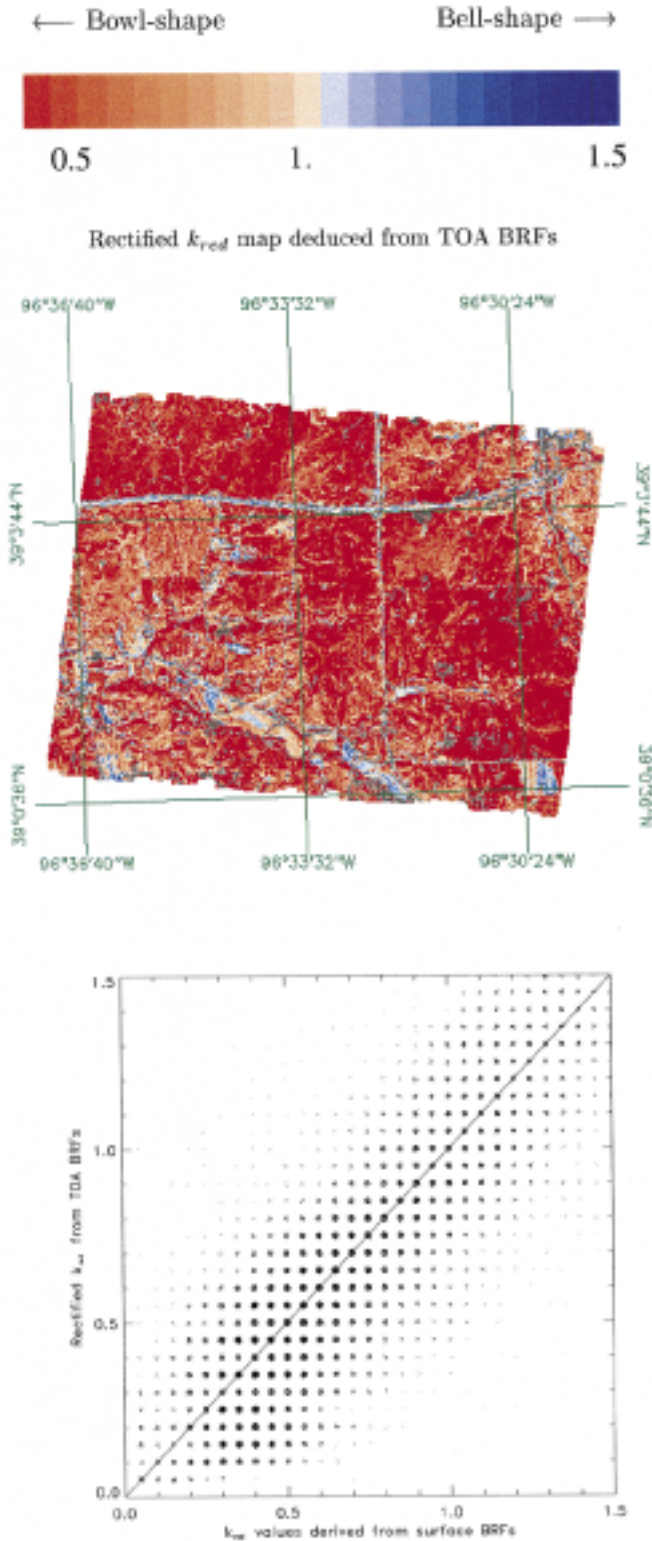
Fig. 7. Top panel shows the map of the k_{red} parameter obtained after applying the rectification procedure on the values estimated, in the red band, from TOA BRFs. The original BRF data set was collected by the AirMISR instrument over the Konza prairie on July 13, 1999. The bottom panel exhibits the histogram of occurrence of couples of values (rectified k_{red} versus surface derived k_{red}). The latter results from the inversion of RPV against the corresponding surface BRF AirMISR data set (see bottom panel of Fig. 5).

is an indicator of structural subpixel heterogeneity induced by the presence of vertical vegetation stands.

III. APPLICATIONS

A. Outline of VEGAS

The VEGetation Activity and Structure (VEGAS) algorithm establishes the state of the vegetation canopy using two independent axes of information: one related to FAPAR (derived from the spectral signature of the surface) and one related to the structure of the geophysical medium (derived from the directional signature of the surface). The complementarity of these two independent approaches is shown graphically in Fig. 8. The mathematics developed in these sections provides the rationale for a simple implementation of the VEGAS algorithm on the basis of the following steps.

- For the Structure axis at 275-m spatial resolution:
  1) inversion of the RPV model against MISR BRF values (using the fast inversion scheme described in Appendix II) in the red band to estimate the values of $k_{\mathrm{red}}^{\mathrm{TOA}}$, the structure parameter, and $\Theta_{\mathrm{red}}^{\mathrm{TOA}}$, the asymmetry parameter;
  2) generation of the rectified k_{red} parameter values [using the polynomial formula in (10)] that best represent the desired $k_{\mathrm{red}}^{\mathrm{SFC}}$ values.

- For the FAPAR axis at 1.1-km spatial resolution:
  1) inversion of the RPV model against BRF values in the blue, red and near-infrared bands to estimate the values of the $\tilde{\rho}_0(\lambda_i)$ corresponding to the optimal value of the amplitude parameter of the BRF field;
  2) generation of the rectified band values (using the polynomial formulae in (5), namely $\rho_{R\mathrm{red}}$ and $\rho_{R\mathrm{nir}}$ for the red and near-infrared bands, respectively;
  3) computation of the FAPAR axis values using $\rho_{R\mathrm{red}}$ and $\rho_{R\mathrm{nir}}$ as input to the polynomial formula in (6).

- For the FAPAR axis at 275-m spatial resolution:
  1) generation of the rectified band values (using the polynomial formulae in (11) and (12) given in Appendix I);
  2) computation of the nadir-only FAPAR axis values using the rectified red and near-infrared band values as input to the polynomial formula in (13) given in Appendix I.

It is worthwhile recalling that the series of spectral and angular coherency tests proposed in Table VI should be performed prior any application of the sequence of computations summarized in this section. In order to avoid rejecting too many cloud contaminated pixels, the angular coherency test procedure we implemented for data collected in the red band follows from the approach suggested in [13]. As such, this procedure checks the angular coherency of the measured BRF fields by attempting to fit the MISR BRF strings with the RPV model, as explained in Appendix II. When the condition ϵ_{fit} is less than the prescribed accuracy ϵ_{wish}, e.g., 10% of the average BRF value, is fulfilled, the process exits the procedure and the BRF series is then interpreted by the sequence of computation proposed previously, as appropriate. Otherwise, the observed BRF value exhibiting the
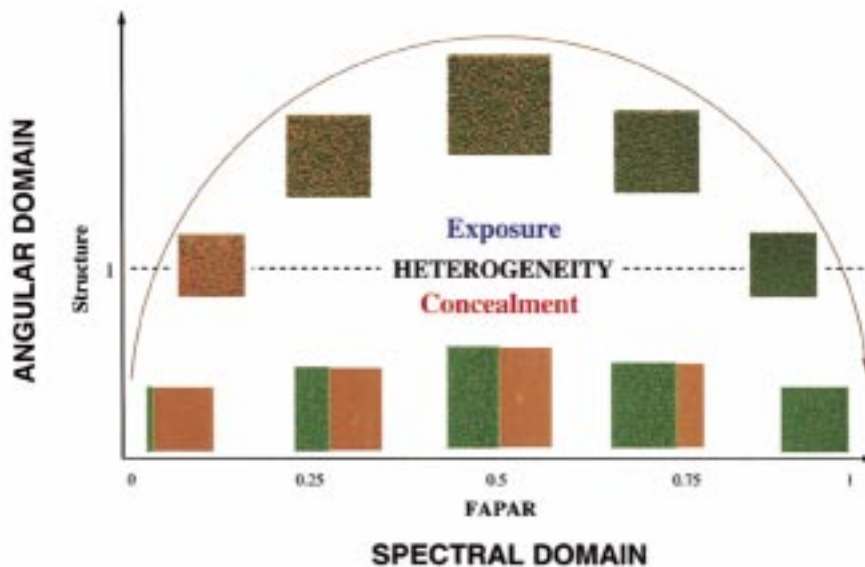
Fig. 8. Conceptual representation of the VEGAS algorithm products. The horizontal axis relates to the photosynthetic activity of the vegetation through an estimate of the FAPAR exploiting the multispectral MISR capabilities. The vertical axis represents the angular shape of the BRF measured in the red MISR band. The domains where subpixel heterogeneity is either exposed or concealed are also indicated together with a sample of panels visualizing some typical surface conditions.

largest absolute departure with respect to the RPV model prediction is eliminated and the series of MISR BRF values is screened again. This iteration procedure is pursued until an acceptable fit is obtained or the number of BRF data points remaining in the series is less than five. This angular coherency procedure guarantees the selection of MISR BRF fields which can be interpreted at a prescribed quality level given by the value of the ϵ_{wish} parameter. It should be underscored that the procedure provides information concerning 1) the identification of clouds and possibly cloud shadows and 2) the detection of inaccuracies in the orthorectification procedure of the original MISR data.

B. Preliminary Application Using MISR Data

The VEGAS algorithm described in Section II has been applied to data collected by MISR over various parts of the globe and this section discusses a sample of the products that have been generated. The main goal of this application is to verify the behavior of the algorithm with respect to the spatial consistency of the retrieved surface products and, if possible, to achieve an intercomparison with independent data sources. The series of spectral tests indicated in Table VI was first used to identify those pixels that are significantly contaminated by the occurence of clouds and/or classified as water bodies. The algorithm was then applied following the procedure explained in Section III-A on several regions including a few selected areas in Northern Europe (the series of Terra orbits available during the month of September, 2000 over paths 196 to 200), Central Africa (Terra orbit 3684 acquired on August 27, 2000 over path 172) and Eastern Australia (Terra orbit 3679 acquired on August 26, 2000 over path 92). All MISR data sets ("beta quality") of each processed orbit were analyzed with the condition $\epsilon_{\text{wish}} \leq 10\%$.

Figs. 9 and 10 illustrate, at a spatial resolution of about 300 m, the spatial variations shown by FAPAR and, over a subregion, the associated RPV-derived parameter values, namely $k_{\text{red}}^{\text{SFC}}$ and $\Theta_{\text{red}}^{\text{TOA}}$, respectively. The quality of the fit of the MISR BRF TOA measurements ϵ_{fit} is also indicated in Fig. 10. In practice, the products were derived using VEGAS for every Terra orbit available in this particular geographical window and selected period of time; they were then remapped onto a geographical grid at about 300-m spatial resolution using a cylindrical projection. Finally, in order to obtain good spatial coverage, we adopted the simple temporal composite procedure described in [8] and [13]. This procedure delivers FAPAR maps on the basis of a time-average composite technique, but it selects the actual, or most representative, day in the time series for which the FAPAR value is the closest to the average. The same time-average technique is applied over the $k_{\text{red}}^{\text{SFC}}$ time series values to establish composited maps of the parameter $k_{\text{red}}^{\text{SFC}}$ and the associated parameter $\Theta_{\text{red}}^{\text{TOA}}$[1] . This procedure ensures that these selected product values are able to represent, at the associated relative accuracy ϵ_{fit}, radiation fields consistent with the multispectral and multiangular BRF samples measured by MISR during the compositing period.

Fig. 9 reveals the different levels of vegetation activity over the variety of surface type and conditions prevailing over the selected region. Specifically, agricultural fields dominate in Denmark whereas forests, including coniferous forest, constitute a major land cover type over Sweden. It can be readily seen that the estimated $k_{\text{red}}^{\text{SFC}}$ values exhibit a spatial pattern which only partly follows that related to vegetation activity. In particular, the largest FAPAR values are correlated with $k_{\text{red}}^{\text{SFC}}$ values

---

[1]If and when only two values are available for the composite period, the most representative day is chosen so that it corresponds to the lowest ϵ_{fit} value.

Fig. 9. FAPAR map constructed after 30-day accumulation period using MISR global mode data in September 2000 over Scandinavia. All Terra orbits available over paths 196 to 200 have been considered. The color bar shows the various classes of FAPAR retrieved. The light blue color identifies pixels flagged as "water body and deep shadow" according to spectral criteria defined in Table VI. The black color identifies pixels for which no solution was delivered by the algorithm. The yellow color identifies pixels flagged as "poor fit of RPV".

which are less than one, indicating the presence of bowl-shaped anisotropy conditions. According to the analysis proposed in Part I, these various features should express different surface cover types and structures. The $k_{\mathrm{red}}^{\mathrm{SFC}}$ values are, as expected from the implemented rectification procedure, systematically lower than the $k_{\mathrm{red}}^{\mathrm{TOA}}$ values. It is interesting to note that the spatial field of the parameter $\Theta_{\mathrm{red}}^{\mathrm{TOA}}$ is pretty smooth over this large region and the average value probably corresponds to rather clear atmospheric conditions. Indeed, this parameter describes the overall asymmetry of the BRF shape which itself depends on the aerosol load, as discussed in Section II-B1. Therefore, the values of the parameter $\Theta_{\mathrm{red}}^{\mathrm{TOA}}$ can be associated with atmospheric turbidity or, more generally, to the density of airborne particulates: the most positive $\Theta_{\mathrm{red}}^{\mathrm{TOA}}$ values being related to the highest atmospheric turbidity conditions.

This latter aspect is better illustrated in Fig. 11 which was derived from an application of VEGAS to MISR measurements acquired over Central Africa during Terra orbit 3684 on August 27, 2000. Indeed, the large north–south gradient observed in the $\Theta_{\mathrm{red}}^{\mathrm{TOA}}$ values (bottom panel) is consistent with an increased aerosol load due to strong fire activities over the northern part of the selected region. Additional work is currently underway to carry out a comparison between the spatio–temporal variations of $\Theta_{\mathrm{red}}^{\mathrm{TOA}}$ and the aerosol amount and type delivered by both the MISR (see [2]) and the MODIS (see [14]) aerosol retrieval algorithm as well as the data acquired by the AErosol RObotic NETwork (AERONET) [15]. Over this region, which shows limited vegetation activity at this time of the year, the associated vegetation structure information (middle panel) appears to be quite variable. Some heterogeneous vegetation pixels, featured by light blue tones, are also exposed in the sense discussed in Part I. Unlike the case for the $k_{\mathrm{red}}^{\mathrm{TOA}}$ parameter values, the north–south gradient observed in the $\Theta_{\mathrm{red}}^{\mathrm{TOA}}$ values does not translate into a similar geographical bias for the $k_{\mathrm{red}}^{\mathrm{SFC}}$ parameter. Therefore, although the RPV model does not guarantee orthogonality between the functions it implements, it seems that
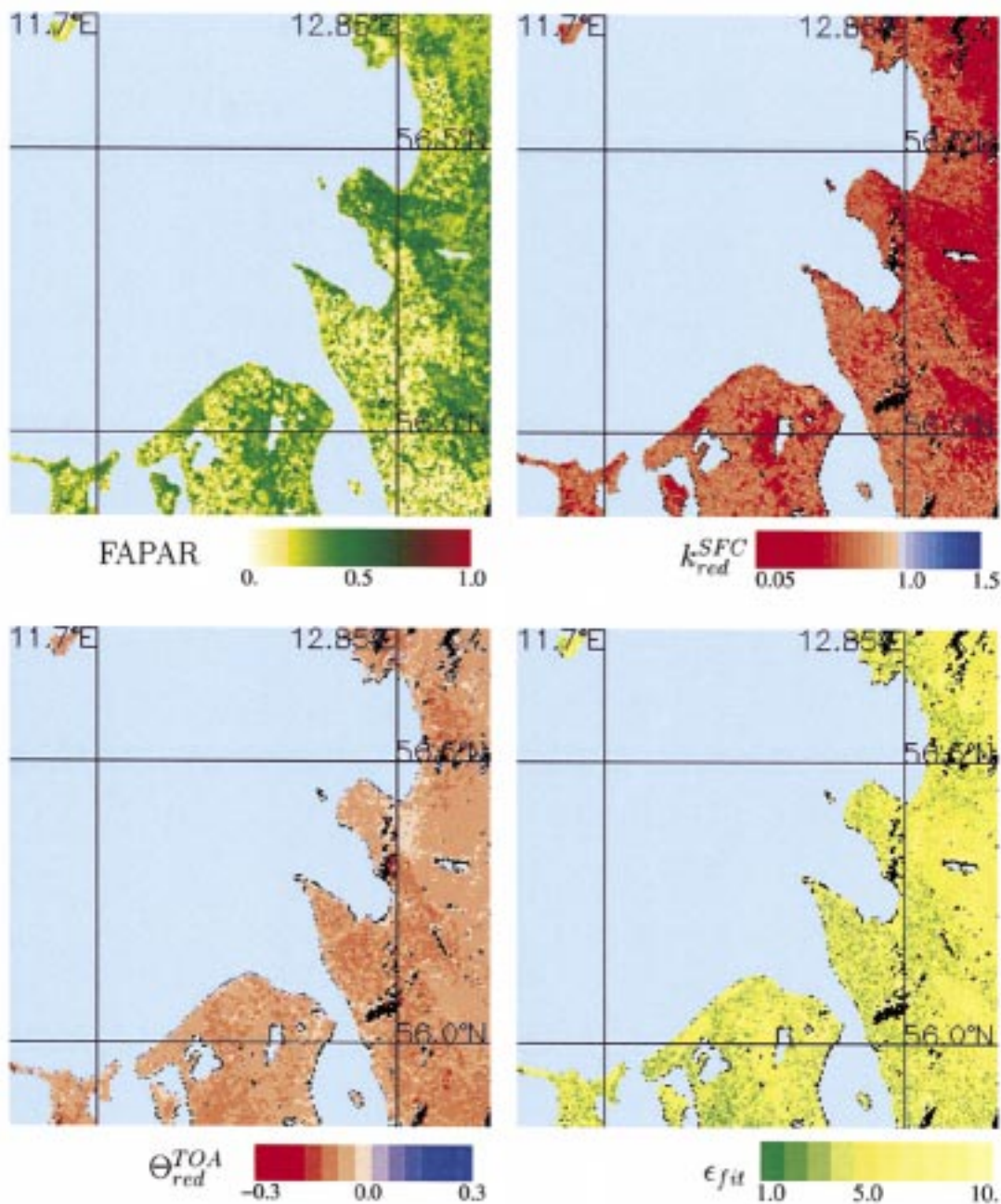
Fig. 10. Maps of the VEGAS products constructed after 30-day accumulation period using MISR global mode data in September 2000 over Scandinavia. All Terra orbits available over paths 196 to 200 have been considered. The top panels are for the FAPAR (left) and $k_{\mathrm{red}}^{\mathrm{SFC}}$ (right) parameters. The bottom panels are for the $\Theta_{\mathrm{red}}^{\mathrm{TOA}}$ (left) parameter and the relative accuracy of the fit ϵ_{fit} (right). The light blue color identifies pixels flagged as "water body and deep shadow" according to spectral criteria defined in Table VI. The black color identifies pixels for which no solution was delivered by the algorithm. The yellow color identifies pixels flagged as "poor fit of RPV".

the decoupling between the k_{red} and Θ_{red} parameter is quite effective.

Figs. 12 and 13 display a series of maps derived from the analysis of MISR data acquired over Queensland (Australia) on August 26, 2000 during Terra orbit 3679. The FAPAR map (Fig. 12) exhibits strong spatial variability corresponding to a wide diversity of vegetation type and structure. A number of these features are related to the vegetation growth form and foliage reported by [16]; for instance, the intense photosynthetic activity in the northwestern part of this map is identified as a re-

gion covered by medium height (10–30 m) trees with more than 70% foliage cover at the tallest stratum. Also, little spots featuring very intense but localized photosynthetic activity in the southern central part of the region are associated with agricultural areas. Fig. 13 illustrates the complexity of the relationships between the vegetation structure, k_{red}, and photosynthetic activity, FAPAR, parameters. Indeed, while FAPAR values show abrupt changes, the k_{red} stays almost constant and its overall spatial field remains quite smooth. The $\Theta_{\mathrm{red}}^{\mathrm{TOA}}$ parameter map exhibits very interesting and complementary features: 1) on top
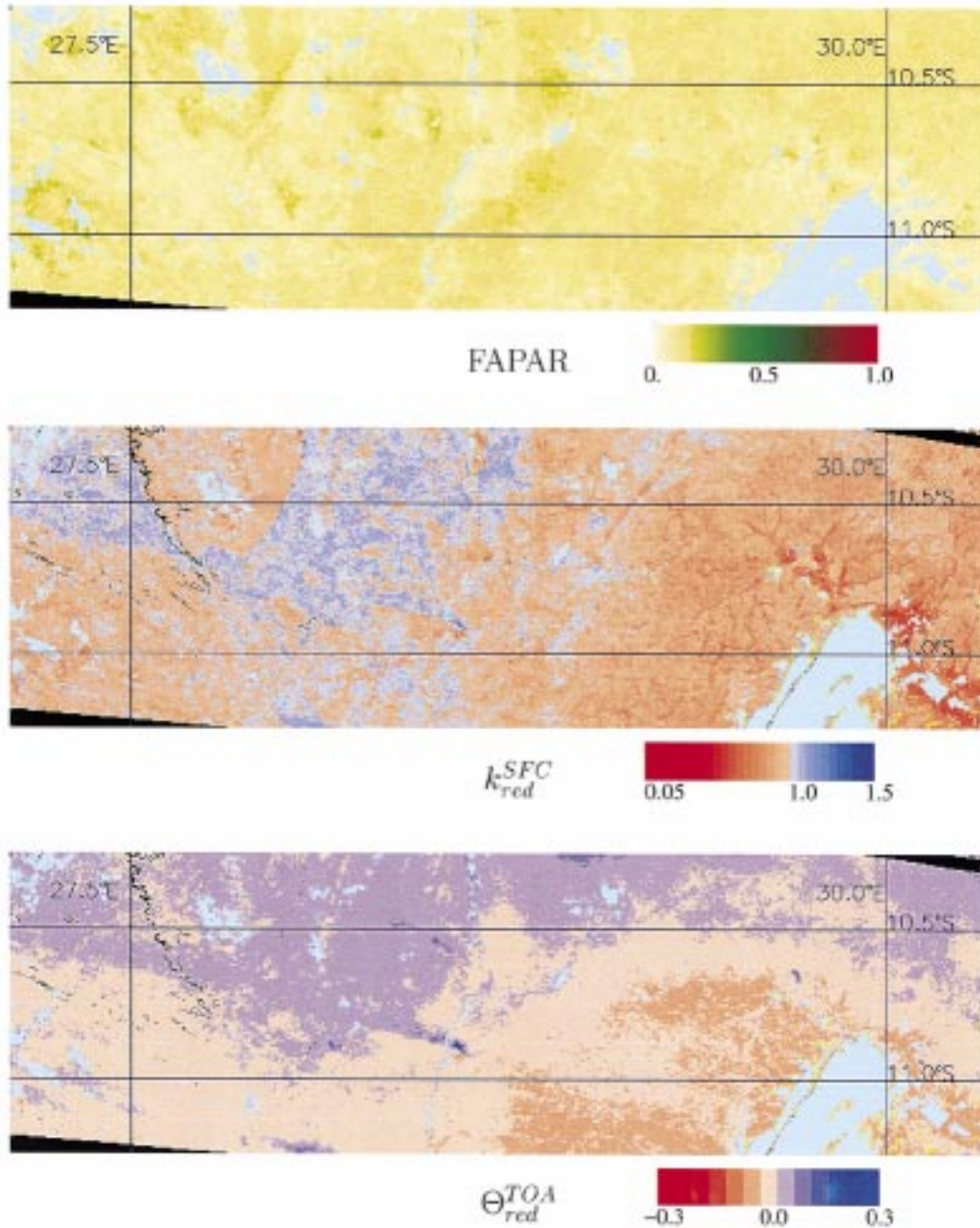
Fig. 11.   Maps of the VEGAS products using MISR global mode data on August 27, 2000 over Central Africa (Terra orbit 3684, path 172). The panels are for (top) FAPAR, (middle) the $k_{\mathrm{red}}^{\mathrm{SFC}}$, and (bottom) $\Theta_{\mathrm{red}}^{\mathrm{TOA}}$ parameters. The light blue color identifies pixels flagged as "water body and deep shadow" according to spectral criteria defined in Table VI. The black color identifies pixels for which no solution was delivered by the algorithm. The yellow color identifies pixels flagged as "poor fit of RPV".

of a spatially smooth background suggesting very low atmospheric turbidity conditions, we can easily locate, in the southwestern part of this region, a sudden increase indicative of a dense aerosol event most probably linked to a local fire and 2) the other increase appearing along the coast fits the location of a littoral complex system, i.e., a mosaic of mangroves or shrubs, identified by [16]. It is noticeable that these spatial variations do not significantly contaminate the FAPAR retrieved values, confirming the robustness of our simple FAPAR algorithm with respect to aerosol effects.

This preliminary application illustrates the potential of the MISR instrument and the proposed VEGAS algorithm to provide simultaneously two complementary axes of information, that is the spectral and the angular domains, to better characterize land surfaces at high spatial resolution. The interpretation of the $\Theta_{\mathrm{red}}^{\mathrm{TOA}}$ parameter needs to be further examined. However, on the basis of straightforward physical considerations and a few examples shown in this section, the analysis of this parameter appears promising for the quantification of atmospheric turbidity and the detection of wetland systems. Basic attributes of
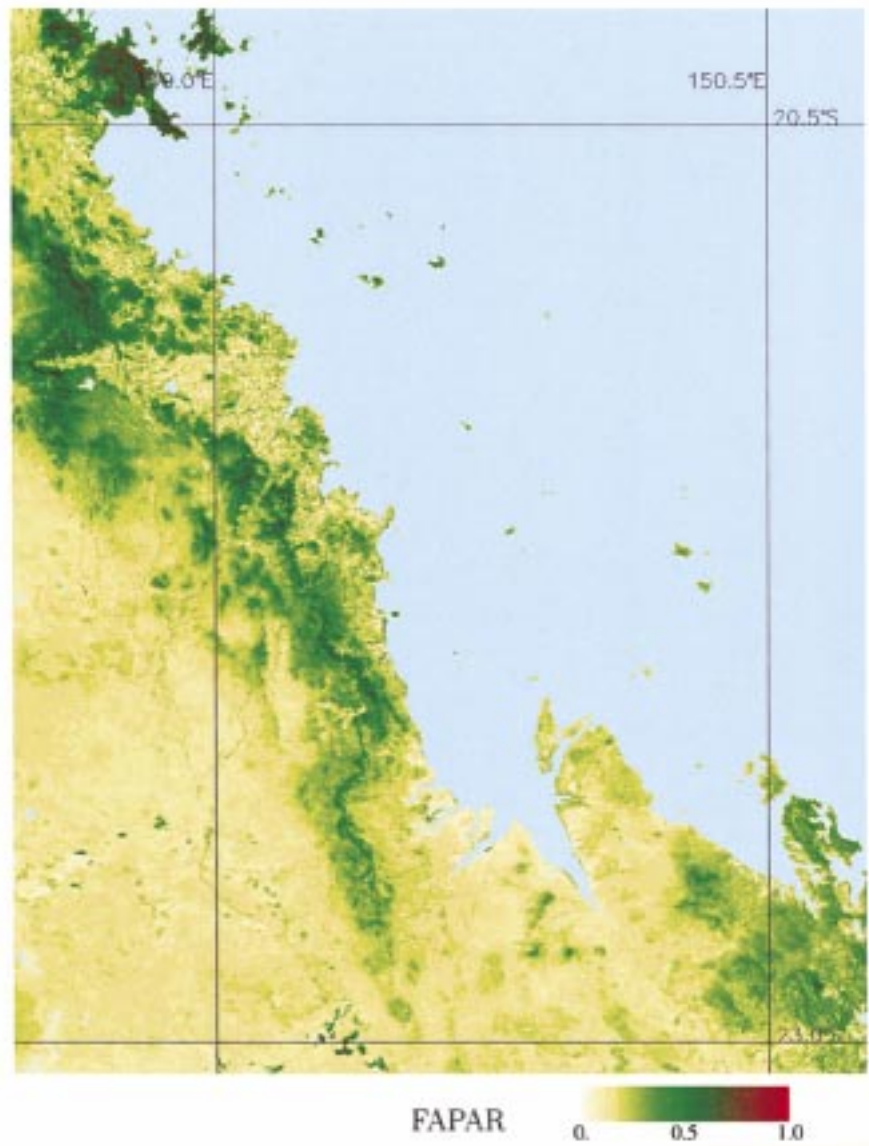
Fig. 12.   FAPAR map derived from MISR global mode data on August 26, 2000 over Queensland (Australia) (Terra orbit 3679, path 92). The color bar shows the various classes of FAPAR retrieved. The light blue color identifies pixels flagged as "water body and deep shadow" according to spectral criteria defined in Table VI. The black color identifies pixels for which no solution was delivered by the algorithm. The yellow color identifies pixels flagged as "poor fit of RPV".

the VEGAS algorithm are its simplicity and low computer demand regarding implementation and operation. It exploits the multiangular and multispectral MISR capabilities and also provides a simple access to advanced surface products from the TOA BRFs acquired by MISR at 275-m and 1.1-km spatial resolution. Many more applications have to be conducted on a systematic basis with this algorithm to better identify its strenghs and weaknesses and to assess its complementarity to the MISR level 2 derived products available at the NASA Langley Atmospheric Sciences Data Center.

IV. GENERAL CONCLUSION

The angular signature of the BRFs emerging from land surfaces and measured from remote sensing techniques in the red spectral region has been coupled with the spectral signature of

these BRFs in the visible/near-infrared domain. The angular signature of interest is expressed simply through a single parameter value entering the RPV BRF parametric model while the spectral signature translates into an estimate of FAPAR.

The angular parameter value is controlled by surface heterogeneity at subpixel resolution and, under some favorable geophysical and measurement conditions, permits detecting the presence of vertical vegetation structures. Based on simple physical reasoning and an ensemble of radiative transfer model simulations, the potential to detect surface heterogeneity at the subpixel scale was confirmed by the analysis of AirMISR data collected during the Konza prairie campaign conducted in June 1999. This new finding demonstrates the unique capability of simultaneous multiangular measurements to document surface structure and architecture [17]. The complementary analysis of spectral variations in the blue, red and near-infrared
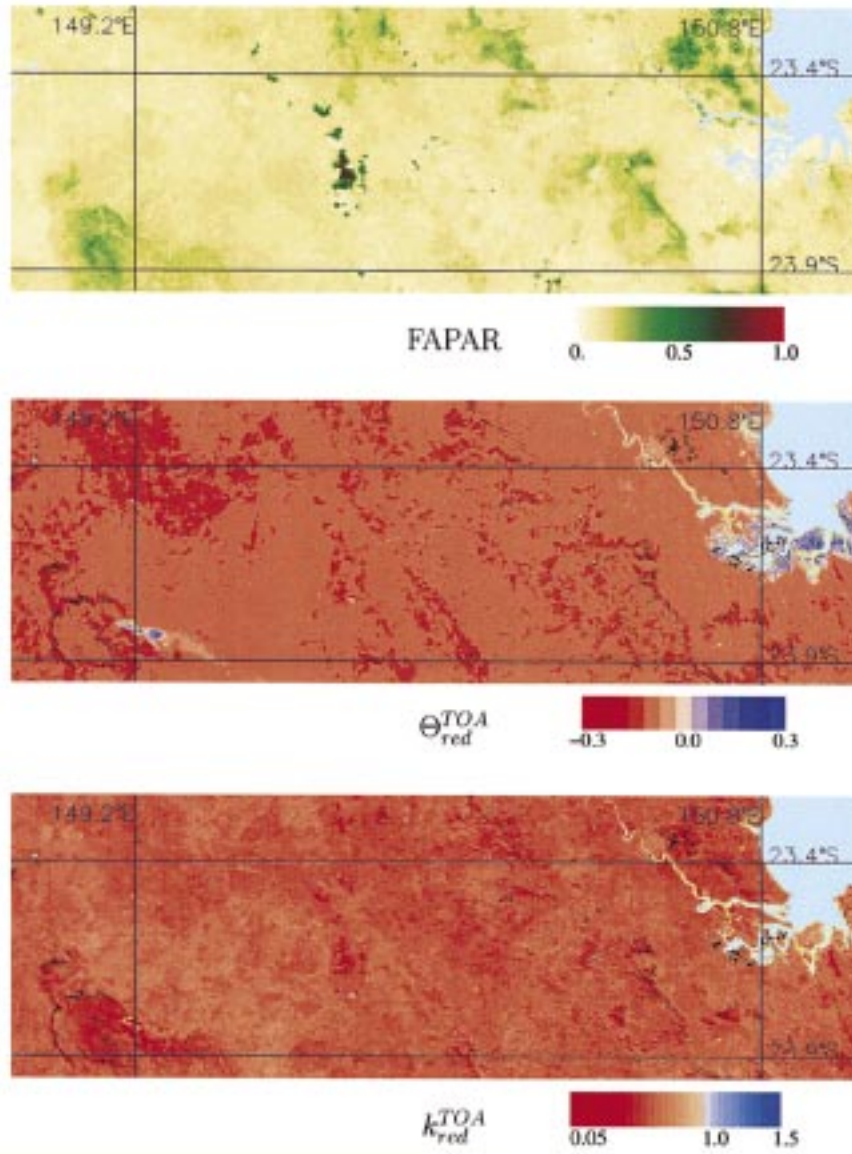
Fig. 13.   Maps of the VEGAS products using MISR global mode data on August 26, 2000 over Queensland (Australia) (Terra orbit 3679, path 92). The panels are for (top) FAPAR, (middle) the Θ_{red}^{TOA}, and (bottom) k_{red}^{TOA} parameters. The light blue color identifies pixels flagged as "water body and deep shadow" according to spectral criteria defined in Table VI. The black color identifies pixels for which no solution was delivered by the algorithm. The yellow color identifies pixels flagged as "poor fit of RPV".

regions has been conducted following a well-defined strategy already in place for the design of optimal spectral indices to estimate FAPAR for various sensors. The most reliable and accurate VEGAS FAPAR algorithm takes advantage of the joint multiangular and multispectral sampling of the instrument at 1.1-km and 275-m spatial resolution. An alternate FAPAR algorithm ingests the near nadir multispectral sampling only to approximate FAPAR at 275-m spatial resolution. These two algorithms proved to be statistically equivalent in the sense that no systematic bias is discernible between the values they deliver, both from model simulations and a sample of actual MISR data over various parts of the globe. These two algorithms should yield, on average, products equivalent to those accessible from single-angle sensors, but the availability of multiangular data is instrumental in increasing the accuracy of the FAPAR estimates. It must be emphasized that the FAPAR

values delivered by this approach can be used in various contexts including qualitative applications usually conducted with classical vegetation indices.

The mapping of surface information must be based on the accumulation of enough data to avoid undesirable atmospheric conditions such as high aerosol load and cloud occurrence. These undesirable conditions can be detected on the basis of a series of multispectral tests, as suggested in Table VI as well as from multiangular tests. The use of appropriate temporal compositing procedures permits us to derive rather geographically complete maps of the VEGAS products over a monthly period. Our preliminary applications indicate that the retrieved vegetation parameters, namely FAPAR and structure, are indeed strongly related to the growth form and foliage cover and, more generally, to the vegetation type. In addition to the two vegetation parameters, this algorithm delivers additional

information about the atmospheric turbidity and the presence of wetland systems.

Extensive intercomparison studies have to be conducted in order to better assess the quality and reliability of the VEGAS products. They should include intercomparison of similar products, such as FAPAR, retrieved from other sensors e.g., MODIS and SeaWiFS, as well as from different algorithms including those implemented in the MISR operational ground segment. Similarly, the potential to assess simply, even on an *ad hoc* manner, the atmospheric turbidity has to be thoroughly investigated and compared against other independent sources of information.

APPENDIX I
A NADIR-ONLY FAPAR AXIS

The following mathematical development describes the approach promoted for the assessment of the presence of vegetation on the basis of the MISR nadir-only measurements available at a resolution of 275 m. It follows from previous investigations made in the cases of a series of single-angle multispectral sensors such as the MERIS [6], the GLI, the VEGETATION [7], and the SeaWiFS [8] instruments. It therefore implements a series of optimizations which permit us to establish the set of polynomial formulae enabling the estimates the red and near-infrared rectified bands as well as the final formula delivering the FAPAR values.

In the absence of documentation of the full angular information in the blue and near-infrared spectral bands, the design of the nadir-only FAPAR algorithm requires assuming the shape of the anisotropy function which enters the optimization procedure. The latter is based on the training data set presented in Table I of this paper and therefore includes a large variety of surface conditions. The geometries of illumination and observation used to simulate the MISR radiance fields are analogous to those already used in Table II, except that the view angles are limited to the nadir, Aa, and Af cameras. The latter two cameras are considered in this exercise, since, in actual applications using terrain-projected radiance fields, the actual view angle of the nadir camera may be slightly off the exact 0° location.

The generic polynomial formula selected for achieving the rectification step of the red and near-infrared band values, namely $h_1(x, y)$ and $h_2(x, y)$ is given by

$$h_n(x, y) = f_n(x, y; q_{(n,1)}, \ldots, q_{(n,m)})$$
$$= \frac{q_{n,1}(x + q_{n,2})^2 + q_{n,3}(y + q_{n,4})^2 + q_{n,5}xy}{q_{n6}(x + q_{n,7})^2 + q_{n,8}(y + q_{n,9})^2 + q_{n,10}xy + q_{n,11}}$$
$$(n = 1, 2). \tag{11}$$

The variables x and y entering polynomial h_1 (h_2) are the normalized BRFs measured in the blue band and those measured in the red (near-infrared) band, respectively. The spectral BRFs are normalized with the appropriate anisotropic reflectance function, namely $\breve{\rho}_i(\Omega; \rho_c, \Theta, k)$ derived from the RPV model (Eq. (1) in Part I), that is

$$\rho_i = \frac{\rho_i(\Omega)}{\breve{\rho}_i(\Omega; \rho_c, \Theta, k)} \tag{12}$$

TABLE VIII
PARAMETER VALUES OF THE RPV FUNCTION $\breve{\rho}_i(\Omega; \rho_c, \Theta, k)$

Band	k	Θ	ρ_c
Blue	0.47	−0.036	0.36
Red	0.82	0.033	0.27
Near-Infrared	0.88	−0.015	0.72

TABLE IX
OPTIMAL VALUES OF THE COEFFICIENTS FOR THE POLYNOMIAL h_1

$q_{1,1}$	$q_{1,2}$	$q_{1,3}$	$q_{1,4}$	$q_{1,5}$
0.5958	4.4888	−20.9020	0.7536	95.9440

$q_{1,6}$	$q_{1,7}$	$q_{1,8}$	$q_{1,9}$	$q_{1,10}$
−0.2552	14.3190	191.8100	−0.4599	1081.6000

$q_{1,11}$
0.0

TABLE X
OPTIMAL VALUES OF THE COEFFICIENTS FOR THE POLYNOMIAL h_2

$q_{2,1}$	$q_{2,2}$	$q_{2,3}$	$q_{2,4}$	$q_{2,5}$
11.7240	−0.11900	0.7426	0.1656	4.6009

$q_{2,6}$	$q_{2,7}$	$q_{2,8}$	$q_{2,9}$	$q_{2,10}$
0	0	0	0	0

$q_{2,11}$
1.0

where $\rho_i(\Omega)$ denotes the simulated (top of atmosphere) BRF in band i available from the training data set at the geometry of illumination and observation noted Ω. The application of this procedure requires *a priori* knowledge on the set of spectral values to be used in the anisotropic reflectance function, namely ρ_c, Θ, and k. The latter values are thus derived, once for all, from the inversion of the RPV model against the ensemble of BRF values generated in the training data set.

The values of the RPV model parameters controlling the anisotropic function and those intervening in the two polynomials h_1 and h_2 are given in Tables VIII–X.

The final polynomial formula adopted for the nadir-only FAPAR formula $h_0(x, y)$ is

$$h_0(x, y) = f_0(x, y; q_{(0,1)}, \ldots, q_{(0,m)})$$
$$= \frac{(q_{0,1}\, y - q_{0,2}\, x - q_{0,3})}{(q_{0,4} - x)^2 + (q_{0,5} - y)^2 + q_{0,6}} \tag{13}$$

and the associated values of the coefficients $q_{(0,1)}, \ldots, q_{(0,m)}$ are provided in Table XI.

TABLE XI
OPTIMAL VALUES OF THE COEFFICIENTS FOR THE POLYNOMIAL h_0

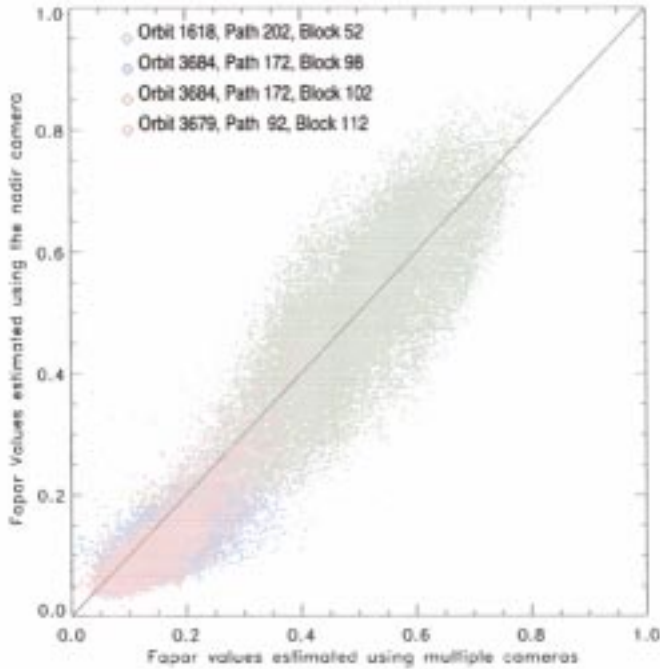| $q_{0,1}$	$q_{0,2}$	$q_{0,3}$	$q_{0,4}$	$q_{0,5}$	$q_{0,6}$
0.3373	0.3253	0.0064192	-0.1867	0.2835	0.07883

Fig. 14. Comparison between the FAPAR values estimated at a spatial resolution of 1.1 km from the formulae using the measurements made simultaneously by the nine MISR cameras and those obtained from the nadir-only FAPAR approach. The color code identifies the measurements used to perform the comparison: block 52 (green tone, orbit 1618 on April 7, 2000), corresponds to the region of Brittany in France, block 98 (blue tone, orbit 3684 on August 27, 2000) is located just south of lake Mweru on the border between Democratic Republic of Congo and Zambia, block 3684 (red tone, orbit 3684 on August 27, 2000) is located in central Zambia and, block 112 (magenta tone, orbit 3679 on August 26, 2000) is located in Queensland, Australia.

The performance of this approach suited to the nadir-only FAPAR information can be examined by comparing its output against those delivered by the set of formulae designed in Section II-A1 exploiting the full multiangular MISR capability. The results of this comparison are illustrated in Fig. 14 for a total of three MISR blocks corresponding to two different paths and for two different orbits. It can readily be seen that, for a large diversity of atmospheric, surface and relative geometries of illumination and observation, the two FAPAR formulae deliver, on the average, analogous values. The scatter of the two FAPAR distribution values which is depicted in Fig. 14 remains within the limits of accuracy inherent to the approach and its corresponding uncertainties, i.e., typically ± 0.1. This scatterplot also reflects the error associated with the assumption of a fixed (i.e., non-biome dependent) shape of the aniotropic function.

APPENDIX II
A FAST INVERSION SCHEME FOR THE RPV MODEL

The following mathematical development reports on a fast inversion scheme of the original nonlinear form of the RPV model [11]. This effort is motivated by the requirement to invert, operationally, this model which has proven to provide better fits over a large variety of geophysical systems than is feasible with a unique linear model but, with the major inconvenience that classical inversion techniques using quasi-Newton or simplex methods present a computing cost which prevents their implementation in operational data processing (see [18]). The aim of the proposed scheme is to control the inversion accuracy by determining the ensemble of solutions or, more realistically, the range of values for the retrieved RPV model parameters. Our scheme therefore uses a χ^2 approach proposed and tested by [19] (see also [20] and [21]) to acknowledge for the uncertainties associated to the input BRF data strings.

For any wavelength location and width, the RPV[2] model parameters can be estimated with the constraint that $\chi^2(\sigma) \leq 1$ where

$$\chi^2(\sigma) = \frac{\sum_{j=1}^{j=N} [\rho^{\text{data}}(j) - \rho^{\text{RPV}}(j; k, \Theta, \rho_0)]^2}{\sum_{j=1}^{j=N} [\sigma(j)]^2} \quad (14)$$

with

$$\sigma(j) = \epsilon_{\text{wish}} \rho^{\text{data}}(j). \quad (15)$$

In (14) and (15), j identifies the individual measurement out of a total on N and ϵ_{wish} the desired accuracy. The inversion constraint can be rewritten as follows:

$$\sum_{j=1}^{j=N} [\rho^{\text{data}}(j) - \rho_0 \, \breve{\rho}(j, \Omega_0 \to \Omega; \rho_c, \Theta, k)]^2 \leq \sum_{j=1}^{j=N} [\sigma(j)]^2 \quad (16)$$

or, in a more compact form:

$$A\rho_0^2 + B\rho_0 + C \leq 0 \quad (17)$$

with

$$A = \sum_{j=1}^{j=N} [\breve{\rho}(j, \Omega_0 \to \Omega; \rho_c, \Theta, k)]^2$$

$$B = -2 \sum_{j=1}^{j=N} \rho^{\text{data}}(j) \breve{\rho}(j, \Omega_0 \to \Omega; \rho_c, \Theta, k)$$

$$C = \sum_{j=1}^{j=N} [\rho^{\text{data}}(j)]^2 - \sum_{j=1}^{j=N} [\sigma(j)]^2. \quad (18)$$

The roots of (17), namely $[\rho_{01}, \rho_{02}]$, can thus be estimated in order to satisfy $\chi^2(\lambda_i, \sigma) \leq 1$ for a set of precomputed values of the $\breve{\rho}(j, \Omega_0 \to \Omega; \rho_c, \Theta, k)$ RPV shape function obtained by varying the k and Θ parameters between predefined limits with given incremental steps. For most applications, a discretization using incremental steps of 0.05 in the range $[0.05, 1.80]$ and

[2]The notations and meaning of the variables are both similar to those already used in Part I [Section II-A, (1)–(7)].

$[-0.5, 0.5]$ for k and Θ parameters, respectively, should be appropriate. Clearly, any incremental steps can be adopted depending on the computer resources that can be assigned to this inversion task.

It is therefore possible to search for the couple $[\rho_{01}, \rho_{02}]$ for any prescribed value of $\sigma(j)$. An alternative also consists in iterating on the value $\sigma(j)$ until at least one couple of roots $[\rho_{01}, \rho_{02}]$ is found. Starting with a first guess value on ρ_c one or two iterations can be performed to force $\rho_c \approx \rho_0$ as originally proposed in [11]. A successful output consists in one or more sets of ρ_0, Θ, and k values which all permit to fit the input data set within the uncertainty level specified by the parameter $\sigma(j)$, i.e., all these sets are statistically equivalent.

For practical purposes it is however generally appropriate to select a single triplet $(\tilde{\rho}_0, \tilde{k}, \tilde{\Theta})$, within this ensemble [13]. If and when such a requirement exists, then the most representative set of the N_c solutions can be selected as the one minimizing the following expression:

$$\delta = |\langle \rho_0(s) \rangle - \rho_0(s)| \tag{19}$$

where $\langle \rho_0(s) \rangle$ represents the mean value estimated as follows:

$$\langle \rho_0(s) \rangle = \frac{1}{N_c} \sum_{s=1}^{N_c} \rho_0(s)$$

$$\rho_0(s) = \frac{1}{2} \left[\rho_{01}(s) + \rho_{02}(s) \right].$$

Once the most representative solution for $\tilde{\rho}_0$ is identified, the associated values of $\tilde{\Theta}$ and $\tilde{k}$ are extracted. This selection gives explicitly more weight to the control of the most representative solution by the value of the amplitude factor of the BRF field.

The main advantage of the RPV model lies in its ability to provide good fits of various geophysical systems on the basis of three parameters only. Its mathematical formula is also appropriate for solving inverse atmospheric problems as shown by [20] and [21]. The inversion procedure described here to retrieve the three RPV parameters is fully compatible with the limited computing costs always associated with an operational environment.

ACKNOWLEDGMENT

REFERENCES

[1] D. J. Diner, J. C. Beckert, T. H. Reilly, C. J. Bruegge, J. E. Conel, R. A. Kahn, J. V. Martonchik, T. P. Ackerman, R. Davies, S. A. W. Gerstl, H. R. Gordon, J.-P. Muller, R. B. Myneni, P. J. Sellers, B. Pinty, and M. M. Verstraete, "Multi-angle imaging spectroradiometer MISR instrument description and overview," *IEEE Trans. Geosci Remote Sensing*, vol. 36, pp. 1072–1087, 1998.

[2] J. V. Martonchik, D. J. Diner, R. A. Kahn, T. P. Ackerman, M. M. Verstraete, B. Pinty, and H. R. Gordon, "Techniques for the retrieval of aerosol properties over land and ocean using multi-angle imaging," *IEEE Trans. Geosci. Remote Sensing*, vol. 36, pp. 1212–1227, 1998.

[3] Y. Knyazikhin, J. V. Martonchik, D. J. Diner, R. B. Myneni, M. M. Verstraete, B. Pinty, and N. Gobron, "Estimation of vegetation canopy leaf area index and fraction of absorbed photosynthetically active radiation from atmosphere-corrected MISR data," *J. Geophys. Res.*, vol. 103, pp. 32 239–32 256, 1999.

[4] N. Gobron, B. Pinty, M. M. Verstraete, J. V. Martonchik, Y. Knyazikhin, and D. J. Diner, "The potential of multi-angular spectral measurements to characterize land surfaces: Conceptual approach and exploratory application," *J. Geophys. Res.*, vol. 105, pp. 17 539–17 550, 2000.

[5] B. Pinty, J.-L. Widlowski, N. Gobron, M. M. Verstraete, and D. J. Diner, "Uniqueness of multi-angular measurements—Part 1: A subpixel surface heterogeneity indicator from MISR," *J. Geophys. Res.*, 2001.

[6] N. Gobron, B. Pinty, M. M. Verstraete, and Y. Govaerts, "The MERIS global vegetation index (MGVI): Description and preliminary application," *Int. J. Remote Sensing*, vol. 20, pp. 1917–1927, 1999.

[7] N. Gobron, B. Pinty, M. M. Verstraete, and J.-L. Widlowski, "Advanced spectral algorithm and new vegetation indices optimized for up coming sensors: Development, accuracy and applications," *IEEE Trans. Geosci. Remote Sensing*, vol. 38, pp. 2489–2505, Nov. 2000.

[8] N. Gobron, F. Mélin, B. Pinty, M. M. Verstraete, J.-L. Widlowski, and G. Bucini, "A global vegetation index for SeaWiFS: Design and applications," in *Remote Sensing and Climate Modeling: Synergies and Limitations*, M. Beniston and M. M. Verstraete, Eds. Dordrecht, The Netherlands: Kluwer, 2001, pp. 5–21.

[9] Y. Govaerts, M. M. Verstraete, B. Pinty, and N. Gobron, "Designing optimal spectral indices: A feasibility and proof of concept study," *Int. J. Remote Sensing*, vol. 20, pp. 1853–1873, 1999.

[10] N. Gobron and D. Lajas, "A new inversion scheme for the RPV model," *Can. J. Remote Sensing*, 2002, in press.

[11] H. Rahman, B. Pinty, and M. M. Verstraete, "Coupled surface-atmosphere reflectance (CSAR) model. 2. Semiempirical surface model usable with NOAA advanced very high resolution radiometer data," *J. Geophys. Res.*, vol. 98, pp. 20 791–20 801, 1993.

[12] C. Leprieur, M. M. Verstraete, and B. Pinty, "Evaluation of the performance of various vegetation indices to retrieve vegetation cover from AVHRR data," *Remote Sensing Rev.*, vol. 10, pp. 265–284, 1994.

[13] B. Pinty, F. Roveda, M. M. Verstraete, N. Gobron, Y. Govaerts, J. Martonchik, D. Diner, and R. Kahn, "Surface albedo retrieval from METEOSAT—Part 2: Application," *J. Geophys. Res.*, vol. 105, pp. 18 113–18 134, 2000.

[14] Y. J. Kaufman, A. Wald, L. Remer, B. C. Gao, R. R. Li, and L. Flynn, "Remote sensing of aerosol over the continents with the aid of the 2.2 μm channel," *IEEE Trans. Geosci. Remote Sensing*, vol. 35, pp. 1286–1298, 1997.

[15] B. N. Holben, T. F. Eck, I. Slutsker, D. Tanré, J.-P. Buis, A. Setzer, E. Vermote, J. A. Reagan, T. Nakajima, F. Lavenu, I. Jankowiak, and A. Smirnov, "Aeronet—A federated instrument network and data archive for aerosol characterization," *Remote Sens. Environ.*, vol. 66, pp. 1–16, 1998.

[16] *Atlas of Australian Resources*, vol. 6, Commonwealth Government Printer, Canberra, Australia, 1990.

[17] J.-L. Widlowski, B. Pinty, N. Gobron, M. M. Verstraete, and A. B. Davies, "Characterization of surface heterogeneity detected at the MISR/TERRA subpixel scale," *Geophys. Res. Lett.*, vol. 28, pp. 4639–4642, 2001.

[18] J. L. Privette, T. F. Eck, and D. W. Deering, "Estimating spectral albedo and nadir reflectance through inversion of simple BRDF models with AVHRR/MODIS-like data," *J. Geophys. Res.*, vol. 102, pp. 29 529–29 542, 1997.

[19] R. Kahn, R. West, D. McDonald, and B. Rheingans, "Sensitivity of multiangle remote sensing observations to aerosol sphericity," *J. Geophys. Res.*, vol. 102, pp. 16 861–16 870, 1997.

[20] J. V. Martonchik, D. J. Diner, B. Pinty, M. M. Verstraete, R. B. Myneni, Y. Knyazikhin, and H. R. Gordon, "Determination of land and ocean reflective, radiative, and biophysical properties using multiangle imaging," *IEEE Trans. Geosci. Remote Sensing*, vol. 36, pp. 1266–1281, 1998.

[21] B. Pinty, F. Roveda, M. M. Verstraete, N. Gobron, Y. Govaerts, J. Martonchik, D. Diner, and R. Kahn, "Surface albedo retrieval from METEOSAT—Part 1: Theory," *J. Geophys. Res.*, vol. 105, pp. 18 099–18 112, 2000.

Nadine Gobron (M'01) received the Maitrise de Physique degree in 1993, the DEA in Sciences de la Terre et de l'Atmosphere degree in 1994, and the doctorat d'universite en Physique de l'Atmosphere in 1997 from the Universite Blaise Pascal, Clermont-Ferrand, France.

She had a Post Doctoral fellowship from ESA in 1998 and JRC in 1999, and was, until 2001, a Staff Member of the Institute for Environment and Sustainability (IES), Ispra, Italy. She has developed physically-based algorithms to retrieve land surface products for instruments of ESA (MERIS/ENVISAT), NASA (SeaWiFS/OrbView-2 and MISR/TERRA), NASDA (GLI), and CNES (VEGTATION). She is an Associate Member of the MISR Science Team. Her main interests currently include the modeling of radiation transfer and the design of advanced methods to extract quantitative information from remote sensing data in the solar domain.

Bernard Pinty received the Maitrise de Chimie and DEA degrees in 1977, the these de troisieme cycle en Physique de l'Atmosphere degree in 1980, and the these d'Etat degree in 1988, all from the Université Blaise Pascal, Clermont-Ferrand, France.

He visited the National Center for Atmospheric Research (NCAR), Boulder, CO, in 1988–1989, served as Deputy Director of the Laboratoire d'Etudes et de Recherches en Teledetection Spatiale (LERTS), Toulouse, France, in 1990–1992, and was appointed Full Professor of physics at the Universite Blaise Pascal in 1993. He is currently with the Institute for Environment and Sustainability (IES), Ispra, Italy. He received the Zel'dovich medal from COSPAR (1990) and is a member of the MERIS Scientific Advisory Group of the European Space Agency, and a member of the MISR Science Team of NASA/JPL. His main interests currently include research on the theory of radiation transfer in plant canopies, and, more generally, the development of tools to quantitatively interpret satellite remote sensing data in the optical spectral domain.

Michel M. Verstraete (M'95) received the License en Physique in 1974 from the Universite Catholique de Louvain, Louvain-la-Neuve, Belgium, the License Speciale en Geophysique in 1976 from the Universite Libre de Bruxelles, Belgium, and the M.Sc. degree in meteorology in 1978 as well as the D.Sc. degree in atmospheric sciences in 1985 from the Massachusetts Institute of Technology, Cambridge.

He worked for the World Meteorological Organization (WMO), Geneva, Switzerland and Nairobi, Kenya, from 1979 to 1981, at the National Center for Atmospheric Research (NCAR), Boulder, CO), from 1982 to 1989, taught at the University of Michigan, Ann Arbor, in 1989–1990, and is currently with the Institute for Environment and Sustainability (IES), Ispra, Italy. He is a member of various scientific advisory committees (e.g., MERIS) of the European Space Agency (ESA) and co-investigator of the MISR Science Team of NASA/JPL. His initial work on topics such as the modeling of atmosphere-biosphere interactions and desertification lead him to his current interest in the quantitative exploitation of satellite remote sensing data for the characterization of terrestrial surface properties.

Jean-Luc Widlowski received the B.Sc. degree in geophysics and planetary physics from the University of Newcastle upon Tyne, U.K., in 1993, the M.Sc. degree in remote sensing and image processing technology from the University of Edinburgh, U.K., in 1995, and the Ph.D. degree from the University of Fribourg, Switzerland, in 2002.

He is currently with the Institute for Environment and Sustainability (IES), Ispra, Italy, developing advanced methods for the extraction of quantitative information on terrestrial surface heterogeneity at the subpixel scale.

David J. Diner (A'01) received the B.S. degree in physics (with honors) from the State University of New York at Stony Brook in 1973 and the M.S. and Ph.D. degrees in planetary science from the California Institute of Technology, Pasadena, in 1977 and 1978, respectively.

He has been with the Jet Propulsion Laboratory, Pasadena, since 1981. He is currently a Principal Member of the Technical Staff and Leader of the Multi-angle Imaging Science Element in the Earth and Space Sciences Division. He has been involved in numerous NASA planetary and Earth remote-sensing investigations, and is Principal Investigator of the MISR experiment and its airborne counterpart, AirMISR.

Dr. Diner is a member of the American Geophysical Union and the IEEE Geoscience and Remote Sensing Society.